RSC Advances

ROYAL SOCIETY OF CHEMISTRY

www.rsc.org/advances

Journal Name

Dynamic Article Links ►

Cite this: DOI: 10.1039/c0xx00000x

www.rsc.org/xxxxxx

ARTICLE TYPE

Graphene-supported small tungsten carbide nanocrystals promoting Pd catalyst towards formic acid oxidation

Chunyong He[a], Juzhou Tao*[a] Yubin Ke[a], Yongfu Qiu[b]*

Received (in XXX, XXX) Xth XXXXXXXXX 20XX, Accepted Xth XXXXXXXXX 20XX
DOI: 10.1039/b000000x

Using a microwave assisting method, we successfully synthesized tungsten carbide nanocrystals of hexagonal prism shape on graphene (WC_P/G). The WC_P nanocrystals are 5 nm in size and dominated by $(01\bar{1}0)$, $(10\bar{1}0)$ and $(1\bar{1}00)$ facets with a preferred orientation of [0001]. An intermittent microwave heating (IMH) method is also utilized to load Pd nanoparicles (NPs) onto WC_P/G to produce Pd-WC_P/G, which displays a significant improvement as catalyst for formic acid oxidation with peak current density increasing by a factor of 7, and notably enhanced durability. We believe this synthesis method of WC_P/G opens new possibilities to research of shape-controlled and high-surface-area transition metal carbide nanocrystals (TMCs) and developing them as efficient and low-cost catalysts or catalyst supports in a broad range of sustainable energy technologies.

Introduction

With the advantages of high energy density, high theoretical open-circuit potential and low fuel crossover, many consider direct formic acid fuel cells (DFAFCs) one of the most promising devices for stationary and portable electronic device applications[1, 2] Oxidation of formic acid is generally accepted to take place through a parallel or dual pathway mechanism:[3-5] 1) the direct dehydrogenation pathway, which involves removal of two hydrogen atoms (dehydrogenation) to form CO_2, $HCOOH \rightarrow CO_2 + 2H^+ + 2e^-$; 2) the indirect dehydration pathway, consisting of a dehydration step to yield water and adsorbed CO, followed by oxidation of CO to CO_2 at high potential, $HCOOH \rightarrow CO_{ads} + H_2O \rightarrow CO_2 + 2H^+ + 2e^-$. Pt and Pd are two of the most effective electrocatalysts for the formic acid oxidation.[6-8] On Pt surface, the formic acid oxidation *via* the indirect pathway is limited by significant amounts of CO as poisoning intermediate accumulating on the catalyst surface and blocking active sites of Pt, whereas the formic acid oxidation on Pd surface proceeds in the direct dehydrogenation pathway to form CO_2.[9-13] This consideration together with its lower cost and higher abundance leads Pd to more research attention recently as the primary catalytic metal. Several approaches exist to further increase the formic acid oxidation efficiency of Pd: 1) alloying to combine the merits of Pd with other metals, including Pd-Pt,[12] Pd−Au,[5, 14] Pd-Cu,[15, 16] and Pd-Ni[17]; 2) building specific shape, architecture and structural arrangement, such as core-shell structure,[18] Pd nanochain networks,[19] three dimensional palladium nanoflowers[20] and Pd nanorods,[21]; 3) developing better catalyst supports to disperse these nanostructures to prevent aggregation and maximize electrocatalytic activity of Pd, with graphene as an excellent choice due to its huge surface area, high electrical conductivity, and excellent catalytic activity;[8, 22] 4) adding co-catalyst to the catalyst system, through which a strong electronic interaction between them may lead to better performance, eg. TiO_2[23] and Ni_2P[24].

Due to similarity of its electronic states to noble Pt at the Fermi level, WC has been studied as catalysts support, as co-catalysts, and as catalyst for oxygen reduction reaction (ORR),[25, 26] methanol oxidation reaction (MOR),[27] formic acide oxidation[28] and hydrogen evolution reaction (HER)[29]. Note that catalytic performance of electrocatalysts is closely related to their shape and configuration, therefore formation of WC nanocrystals with controllable shape and structure is of considerable research interests. Previously WC nanorods through size-controlled hydrothermal reaction of WO_3 nanorods,[30] mesoprous WC/C by a hydrothermal reaction route,[31] and WC nanowall using high-vacuum chemical vapor deposition were reported.[32] However, it was not facile to obtain small WC nanocrystals (especially sub-10 nm) with controllable morphology and structure.

In this paper, we present synthesis of tungsten carbide nanocrystals with hexagonal prism shape on graphene (WC_P/G) *via* a novel microwave assisting method. The WC_P nanocrystals, of 5 nm in size, are dominated by $(01\bar{1}0)$, $(10\bar{1}0)$ and $(1\bar{1}00)$ facets with a preferred orientation of [0001]. The WC_P/G shows a

Journal Name

Dynamic Article Links ►

Cite this: DOI: 10.1039/c0xx00000x

www.rsc.org/xxxxxx

ARTICLE TYPE

remarkable promotion for formic acid oxidation when coupled with Pd nanoparticles (Pd NPs). Compared to Pd/C, both catalytic activity as indicated by peak current density and durability of Pd-WC_P/G improved dramatically.

Experimental

Synthesis of hexagonal prism tungsten carbide nanocrystals on graphene (WC_P/G)

Graphite oxide (GO) powders were prepared *via* the modified Hummers method through oxidation of natural graphite powders (325 mesh, XFNANO Material Technologic Co. Ltd., Nanjing, China). 1.6 g GO powder was first dissolved in 200 mL DI water and turned into (graphene oxide sheets) suspension after 2 h of ultrasonic agitation. Add ammonium metatungstate (AMT, 0.33 g) into the suspension and continue mixing at 80 °C until the dispersed ink dried. Then the dried powders were loaded into a microwave oven (2,000 W, 2.45 GHz, CNWB, Guangzhou Wangcheng Microwave Equipment CO., LTD) and underwent the microwave heating for 2 min, followed by intermittent microwave heating (IMH, 15 s-on/15 s-off) for 15 cycles. This IMH method has previously been used to synthetize small size and uniformly dispersed WC nanocrystals.[26]

Preparation of Pd-WC_P/G

Pd-WC_P/G catalyst was prepared *via* adsorption/reduction also using the IMH method and described as follows. Palladium (II) sodium chloride precursor (7.2 ml, 9.2 mg_{Pd} ml^{-1}) was first well mixed with ethylene glycol (EG, 50 ml) in an ultrasonic bath. Then, the WC_P/G (100 mg) was added into the mixture. The pH of the mixture was further adjusted to 10 using 0.1 mol L^{-1} NaOH/EG solution. After stirring and ultrasonication for 30 min, the mixture was microwave-heated in 5 s-on/5 s-off cycle for 20 times. The resulting black solid sample was acidified, filtered, washed and dried at 80 °C for 12 h in a vacuum oven.

For comparison Pd on VC-72 (Pd/C) was also prepared using the same method and under the same conditions.

Characterizations

X-ray diffraction (XRD) analysis was performed on a D/Max-III (Rigaku Co., Japan) operating at 30 kV and 30 mA using Cu Kα radiation, 2θ angular ranges between 10° and 80°/90° were measured at a scan rate of 6° min^{-1}. Raman spectroscopic measurements were carried out on a Raman spectrometer (Renishaw Corp., UK) using a He/Ne laser at 514.5 nm wavelength. Structural and morphological characterizations were conducted on a field emission transmission electron microscopy (FETEM, FEI Tecnai G2 F30) operating at 300 kV. High-angle annular dark-field scanning transmission electron microscopy-energy dispersive spectroscopy (HAADF-STEM-EDS) elements mapping analyses were also performed with the same instrument at 300 kV.

Pd *K*-edge X-ray absorption spectroscopy (XAS) of Pd foil, Pd/C and Pd-WC_P/G in transmission and total electron yield mode were recorded at the beamline BL14W1 of the Shanghai Synchrotron Radiation Facility (SSRF). XAFS data were collected using a fixed-exit double-crystal Si(311) monochromator. A 32-element Ge solid-state detector was used to collect the fluorescence signal, and the energy was calibrated using Pd foil and a third ionization chamber. Photon flux at the sample position was 7.2×10^{11} photons per second. All data were subjected to background correction using Athena (IFFEFFIT software package) followed by single shell EXAFS fitting analyses using the Artemis program.

Electrochemical measurements

A Bio-logic VMP3 electrochemical work station (France) was employed to perform electrochemical measurements in a thermostat-controlled standard three-electrode cell at 30 °C with a saturated calomel electrode (SCE) as reference electrode and a platinum foil (1.0×1.0 cm^{-2}) as counter electrode. The formic acid oxidation of the Pd-WC_P/G electrocatalyst was carried out in nitrogen-saturated 0.5 mol L^{-1} H_2SO_4 containing 1.0 mol L^{-1} HCOOH solution. The cyclic voltammograms (CVs) were collected at a scan rate of 0.02 V s^{-1} within a potential window of -0.2 to 0.96 V *vs.* SCE. Durability of the Pd-WC_P/G for formic acid oxidation was measured performing CVs of Pd-WC_P/G over 2,000 cycles at a scan rate of 0.1 V s^{-1} from -0.2 V to 0.96 V.

The catalyst ink of Pd/C was also prepared and measured for comparison. 5.0 mg catalysts (Pd-WC_P/G or Pt/C) and 0.5 mL Nafion solution (0.05 wt %, DuPont, USA) solution were dispersed in 0.5 ml of ethanol by sonication for an hour to form well-dispersed ink. A certain amount of the ink was transferred onto surface of glass carbon electrode. Drying under infrared lamp for 5 min produced desired catalyst thin films.

Results and Discussions

Black curve in Fig. 1 is the XRD pattern of WC_P/G and indicates formation of tungsten monocarbide (WC). Peaks at the 2θ of 31.51°, 35.64°, 48.30°, 64.02°, 73.10° and 77.10° have *d* values of 2.8431Å, 2.5170 Å, 1.8813 Å, 1.4531 Å, 1.2934 Å and 1.2360 Å corresponding to (001), (100), (101), (110), (111) and (102) reflections of WC crystal, respectively The diffraction peak at 2θ=26.2° is the characteristic graphite (002) reflection.

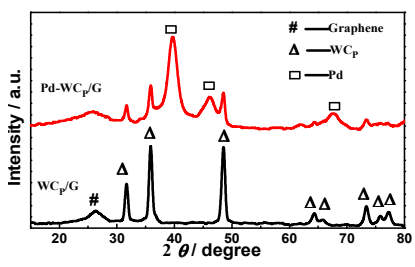

Fig. 1 The XRD pattern of tungsten carbide/graphene (WC_P/G) (black curve) and Pd nanoparticles supported on WC_P/G (Pd-WC_P/G) (red curve).

Journal Name

Dynamic Article Links ►

Cite this: DOI: 10.1039/c0xx00000x

www.rsc.org/xxxxxx

ARTICLE TYPE

Morphology and structure of WC_P/G were studied by TEM, with a typical image shown in Fig. 2a. The WC_P nanocrystals dispersed on graphene sheets uniformly with no agglomeration. Fig. 2b displays high magnification TEM image of WC_P/G and the hexagon shape of WC_P nanocrystals. Some WC_P nanocrystals show regular hexagons with adjacent equal length edges, while others display parallelogons with unequal adjacent edges. According to particle size distribution of Fig. 2c, average particle size is about 5 nm, one of the smallest WC sizes reported in the literatures so far.[33] The crystal structure of the WC_P was further analyzed by high-resolution TEM (HRTEM). Fig. 2d-f show the HRTEM images of three WC_P nanocrystals marked in Fig. 2b. The lattice-resolved TEM images correspond to $(01\bar{1}0)$, $(10\bar{1}0)$ and $(1\bar{1}00)$ facets of WC_P nanocrystals, respectively, which can only be observed when the nanoparticles are oriented along [0001]. The FFT patterns (Fig. 2g-2i) recorded from the HRTEM images are also consitently indexed according to the hexagonal structure (P-6m2(187)), which confirm the structural analysis of HRTEM. Atomic rearrangement disorder and defects on the surfaces of WC_P, indicated by red arrows in Fig. 2d-f, were also identified, likely due to the short synthesis duration and not enough time for the nanoparticles to achieve perfect crystal structure.[34, 35] Surface structure changes of catalysts usually result in alternations of electronic properties, strain, and bonding factors, which may actually benefit their performance in electrochemical applications.[14]

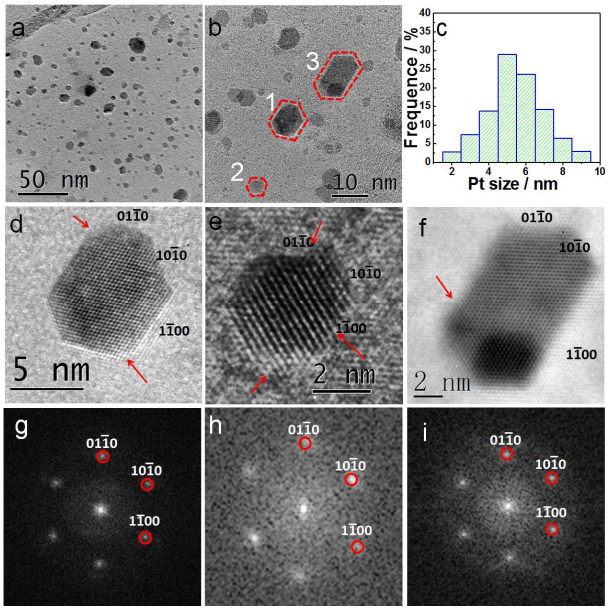

Fig. 2 (a,b) TEM image of WC_P/G, (c) the corresponding size-distribution histogram of the WC_P nanocrystals, (d-f) HRTEM images of WC_P nanocrystals oriented along [0001], (g-i) the corresponding fast Fourier transformation (FFT) patterns.

To identify the three-dimensional morphology and investigate the composition of WC_P/G, high-angle annular dark-field scanning transmission electron microscopy (HAADF-STEM) and X-ray element analysis were carried out (Fig. 3). HAADF-STEM images of WC_P/G (Fig. 3a and 3b) show the WC_P nanocrystals homogenously dispersed on the graphene support. The WC_P nanocrystals have a mean diameter of approximately 5 nm, in agreement with the TEM result. The atomic-resolution HAADF-STEM image recorded from two individual WC_P nanocrystals as shown in Fig. 3c further reveals the morphology of WC_P nanocrystal hexagon. Fig. 3d shows a close-up of the WC_P nanocrystal extracted from the red hexagon area oriented along [0001]. Its inset of the corresponding FFT pattern also identifies the $(01\bar{1}0)$, $(10\bar{1}0)$ and $(1\bar{1}00)$ lattice facets, consistent with the TEM result.

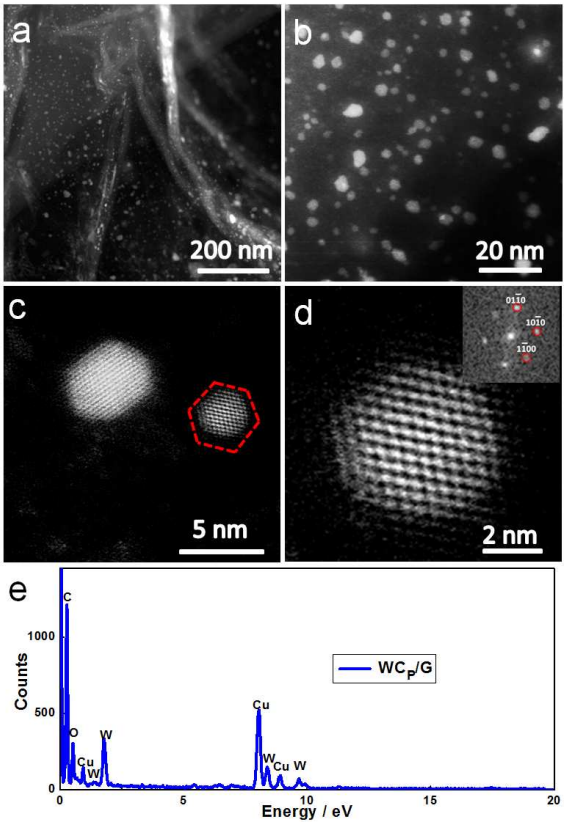

Fig. 3 (a,b) HAADF-STEM image of WC_P/G, (c) atomic-resolution HAADF-STEM image of WC_P nanocrystals, (d) a close-up of the WC_{THP} nanoparticle extracted from the red hexagon area oriented along [0001]. The inset is the corresponding FFT pattern, (e) the EDS pattern of WC_P/G.

The HAADF-STEM signal originates from electron scattering

Journal Name

Dynamic Article Links ►

Cite this: DOI: 10.1039/c0xx00000x

www.rsc.org/xxxxxx

ARTICLE TYPE

by atomic nuclei, which is proportional to the thickness of specimen and to the atomic mass of atoms in the sample.[36, 37] In our case, the HAADF-STEM intensity corresponds to the thickness profile of the WC_P nanocrystals and contains 3D crystalline structure information of the WC_P nanocrystals. Fig. 4a shows atomic-resolution HAADF-STEM image of an individual WC_P nanocrystal oriented along [0001]. Fig. 4b illustrates a model of the electron beam incident on the WCp nanocrystal. Three intensity profiles acquired along different directions perpendicular to the major axis (indicated in Fig. 4a) are shown in Fig. 4c-e. The isosceles trapezoid shapes of the intensity profiles clearly indicate that the morphology of the WC nanocrystals is indeed hexagonal prism.

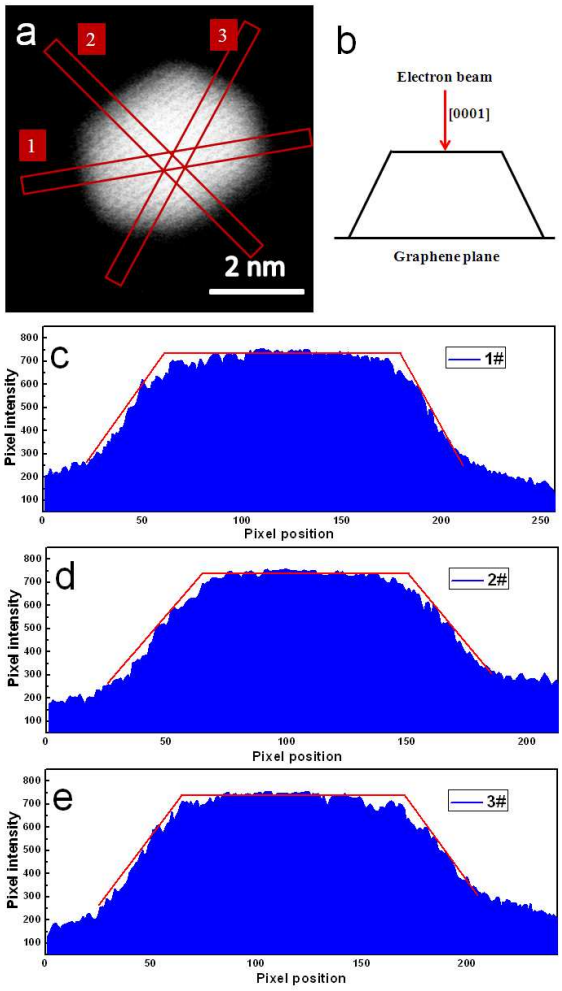

Fig. 4 (a) Atomic-resolution HAADF-STEM image of a single WC_P nanocrystal oriented along [0001], (b) model of WC_P nanocrystal on graphene plane surface, (c-e) intensity profiles acquired from each of the three numbered zones marked in red in (a).

The Raman spectra of GO, WC_P/G and Pd-WC_P/G were collected to reveal bonding state and structure of carbon atoms in graphene. Fig. 5 shows comparison of Raman spectra among GO, WC_P/G and Pd-WC_P/G in the range of 1000–2000 cm^{-1}. The D band at 1350 cm^{-1} characterizes the disordered graphite planes and the defects incorporated into pentagon and heptagon graphitic structures.[38] The G band, observed at about 1577cm^{-1} reflects the structural intensity of sp^2-hybridized carbon atoms.[39] The intensity ratio of G-band to D-band (I_G/I_D) is often used to characterize degree of crystallinity of the carbon material studied,[40] which are 0.78, 1.47 and 1.52, respectively, for GO, WC_P/G and Pd-WC_P/G. This observed increase of the I_G/I_D ratios indicates a significant increase in structure ordering of graphene sheets and a higher degree of crystallinity for graphene carriers, which is necessary to the durability of the catalyst system. In our experiments, the GO was reduced during the microwave heating processes. In the high temperature environment produced by microwave heating, the hydroxyl and carboxyl groups on the GO sheets were removed in gaseous phase (CO_2 and H_2O (g)), the GO sheets recovered their graphitic structure. So the WC_p/G and Pd-WC_p/G samples have better graphitic structure than GO. Hence, the I_G/I_D of WC_P/G and Pd-WC_P/G increase compare with the GO.

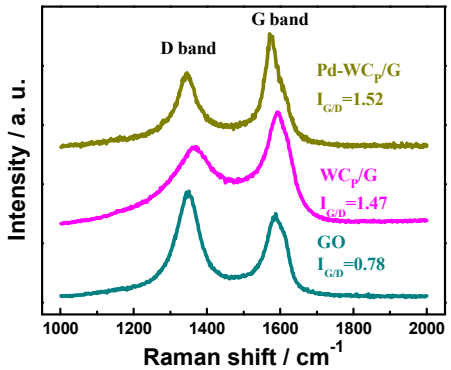

Fig. 5 Raman spectra of the GO, WC_P/G and Pd-WC_P/G.

Fig. 1 (red curve) also dislays the XRD pattern of the Pd-WC_P/G, showing the Pd and WC phases unambiguously. The broad peak at around 26.2° again originates from the graphene support. The four peaks at 40°, 46°, 68°are assigned to the (111), (200) and (220) crystalline planes of the face centered cubic (fcc) structured Pd (JCPDS No. 46-1043), respectively. Fig. 6a shows the typical TEM image of the Pd-WC_P/G. Pd nanoparticles with the approximate size of 3 nm are uniformly distributed on the WC_P/G support. Fig. 6b displays the HRTEM image of the Pd-WC_P/G nanoparticle marked by the red box in Fig. 6a, the blue dotted rings represent Pd nanoprtices, the red

Journal Name

Dynamic Article Links ►

Cite this: DOI: 10.1039/c0xx00000x

www.rsc.org/xxxxxx

ARTICLE TYPE

dotted parallelogon is WC_P nanocrystal. The close attachment of the Pd nanoparticles to the WC_P nanocrystal suggests a strong interaction between the Pd and WC_P, which is expected to produce synergistic effects between Pd and WC_P for enhanced catalytic activity. Fig. 6c shows the HAADF-STEM image of Pd-WC_P/G nanocomposite, it is clear that the Pd nanoparticles stuck on both surfaces of the WC_P nanocrystals and graphene sheets. Fig. 6d and 6e show the elemental mapping analysis of W and Pd, respectively. The mapping results confirm the tight attachment between the Pd and WC_P, in agreement with the HRTEM and HAADF-STEM analysis. It should be noted that there are some some other Pd nanoparticles just loaded on the graphene sheets without contaction with WC_P since the graphene sheeets are not bespread by WC_P and the Pd nanoparticles dispersed homogeneously on the WC_P/G. The EDS pattern (Fig. 6f) also confirms the co-existence of Pd and W in the Pd-WC_P/G.

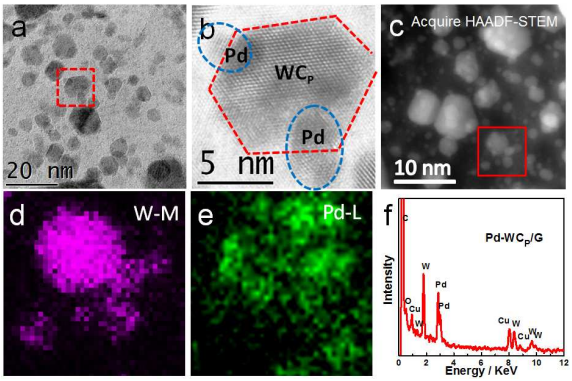

Fig. 6 (a) Typical TEM image of Pd-WC_P/G, (b) HRTEM image of the Pd-WC_P/G acquired from the red box in (a), (c) HAADF-STEM image of Pd-WC_P/G, (d,e) HAADF-STEM-EDS elemental mapping images of the Pd-WC_P/G obtained from an area marked in red box in c, (f) EDS pattern of the Pd-WC_P/G.

Catalytic properties of the as-prepared Pd-WC_P/G were investigated using formic acid oxidation as the representative and Pd/C as well as Pt/C for comparison. Fig. 7a shows the cyclic voltammograms (CVs) of Pd/C, Pd-WC_P/G and Pt/C recorded in 0.5 mol L^{-1} H_2SO_4 at 20 mV s^{-1}. Hydrogen adsorption/desorption peaks occurred for Pt/C in the range -0.2 to 0.1 V (*vs.* SCE), and were used to evaluate the electrochemical surface area (ECSA), which is calculated by measuring charge collected in the hydrogen adsorption/desorption regions after double-layer correction and assuming a value of 210 μC cm^2 for the adsorption of a hydrogen monolayer.[26, 41] For Pd/C and Pd-WC_P/G however, the peaks in the range -0.2 to 0 V (*vs.* SCE) attributed to respective hydrogen adsorption, desorption and evolutio are not well-separated and therefore not appropriate for evaluating the ECSA, which were instead estimated by the oxygen adsorption method and shows well-developed regions for oxide monolayer formation and reduction (the charge is 424 μC cm^2).[20, 42] In Fig. 7a, the cathodic curves of the Pd/C and Pd-WC_P/G present Pd surface oxide reduction peaks at 0.50 and 0.47 V. The ECSA of the Pd/C, Pd-WC_P/G and Pt/C are 21.1, 34.5 and 48.1 m^2 g_{metal}^{-1}, respectively.

The formic acid oxidation performances of the Pd/C, Pd-WC_P/G and Pt/C are shown in Fig. 7b. It can be seen that the CVs profiles of Pd/C and Pd-WC_P/G are different from Pt/C. For Pd/C and Pd-WC_P/G, prominent peaks ranging from −0.1 to 0.5 V correspond to formic acid oxidation *via* the direct pathway (dehydrogenation reaction, $HCOOH \rightarrow CO_2 + 2H^+ + 2e^-$).[17, 43] On the other hand the prominent peak of Pt/C ranges from 0.6 to 0.8 V, indicating the formic acid oxidation on Pt/C *via* the indirect pathway (dehydration reaction, $HCOOH \rightarrow CO_{ads} + H_2O \rightarrow CO_2 + 2H^+ + 2e^-$).[44] The peak current densities of the three electrodes are 435 mA mg^{-1}_{metal}, 3062 mA mg^{-1}_{metal} and 370 mA mg^{-1}_{metal} for Pd/C, Pd-WC_P/G and Pt/C, respectively. The Pd-WC_P/G exhibits about 7-fold enhancement in mass activity compared to the Pd/C and more than 8-fold to Pt/C. Fig. 7c displays the comparison of specific activities (j_k, obtained by normalizing the electrode current to the ECSA) of Pd/C, Pd-WC_P/G and Pt/C. The Pd-WC_P/G exhibits about 4-fold enhancement in specific activity compared to the Pd/C at 0.25 V (*vs.* SCE).

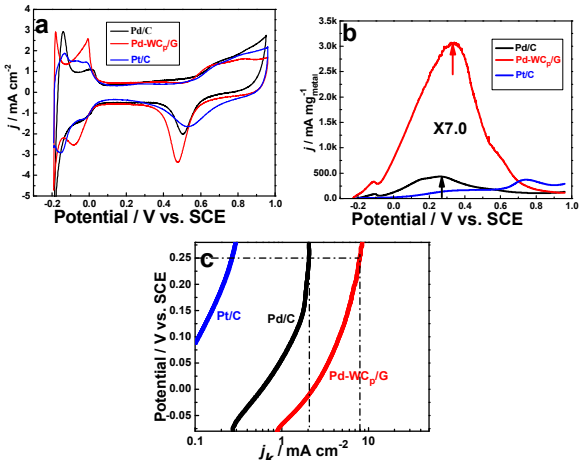

Fig. 7 (a) Typical cyclic voltammograms (CVS) of Pd/C, Pd-WC_P/G and Pt/C in N_2-saturated 0.5mol L^{-1} H_2SO_4 with the scan rate of 20 mV s^{-1} at 30℃, (b) CVs recorded at 20 mV s^{-1} of Pd/C, Pd-WC_P/G and Pt/C in 0.5 mol L^{-1} H_2SO_4 + 1.0 mol L^{-1} HCOOH solution, (c) comparison of specific activities.

In the process of formic acid oxidation, an indistinct shoulder at potential range from 0.6 to 0.8 V were observed on the Pd/C and Pd-WC_P/G electrodes, which implies a very small portion of formic acid will be oxidated *via* the indirect dehydration pathway. The poisonous CO_{ads} generated from formic acid oxidation accumulates on electrocatalyst surface and reduce its electrocatalytic activity. The anti-poisoning abilities of

Journal Name

Dynamic Article Links ►

Cite this: DOI: 10.1039/c0xx00000x

www.rsc.org/xxxxxx

ARTICLE TYPE

the electrocatalysts were evaluated by a steady-state measurement, with respective chronopotentiometric curves of formic acid oxidation on Pd/C, Pd-WC_P/G and Pt/C electrodes at a current density of 5 mA cm^{-2} shown in Fig. 8a. On the Pt/C electrode, the potential oscillation appeared during constant current polarization, indicating deterioration and poisoning due to the formation of CO_{abs} on the platinum surface, which needs higher potential to oxidize the CO_{abs} and release a clean surface.[45, 46] When the electrocatalyst becomes heavily poisoned, the formic acid oxidation reaction cannot continue. The chronopotentiometric curves of formic acid oxidation on Pd/C and Pd-WC_P/G are smooth, confirming formic acid oxidation on Pd/C and Pd-WC_P/G *via* the direct pathway with no obvious poisonous species CO_{abs} on the surfaces. The potential to satisfy the identical applied anodic current density on Pd-WC_P/G is lower than Pd/C and Pt/C, implying higher output voltage and power density. The time (*T*) that the catlyst can sustain activity for formic acid oxidation at low overpotential is introduced to evaluate the anti-poisoning ability of catalysts. Based on the corresponding data in Fig. 8a, the *T* values increase in this order: Pd-WC_P/G (>600 s) > Pd/C (234 s) > Pt/C (190 s). The above results demonstrate that the Pd-WC_P/G catalyst exhibits better electrocatalytic properties and better resistance to poisoning than the Pd/C and Pt/C catalysts.

Pd-based catalysts during oxidation of formic acid deactivates through gradual build-up of adsorbed poisonous species CO_{abs} on the Pd surface blocking catalytic active sites.[47] The presence of residual oxygen functional groups on graphene sheets prepared through chemical reduction (RGO) have been found benefitial to the removal of the adsorbed poisonous species CO_{abs} from the adjacent Pd sites *via* a bifunctional mechanism.[48, 49] This mechanism of promoted CO_{abs} oxidation on the active Pd sites is described as:

$$RGO + H_2O \rightarrow RGO\text{-}(OH)_{ads} + H^+ + e^- \quad (1)$$

$$Pd\text{-}CO_{ads} + RGO\text{-}(OH)_{ads} \rightarrow CO_2 + Pd + RGO + H^+ + e^- \quad (2)$$

To study long-term performance of electrocatalysts, we measured chronoamperometric (CA) profiles of formic acid oxidation on Pd/C, Pd-WC_P/G and Pt/C catalysts at 0.1 V (*vs.* SCE) for 1600 s in N_2-saturated 0.5 mol L^{-1} H_2SO_4 solution containing 1.0 mol L^{-1} HCOOH, as shown in Fig. 8b. All electrodes displayed an initial obvious current decay followed by a slower attenuation upon longer-time operation, before reaching a quasi-equilibrium steady state. The degeneration of the electrodes is attributed to diffusion and mass transfer, and the formation of the poisonous species CO_{abs}. The current decay rate of Pd-WC_P/G is much slower than Pd/C. After 1600 s of polarization, the Pd-WC_P/G still exhibited a current densitie of 339.0 mA mg^{-1}_{metal}, whereas the Pd/C electrode only left 94.1 mA mg^{-1}_{metal}. The long-term stability of Pd-WCp/G is consistent with the view that the presence of residual oxygen functional groups on graphene sheets can promote the oxidation of CO_{ads} on the active Pd sites.

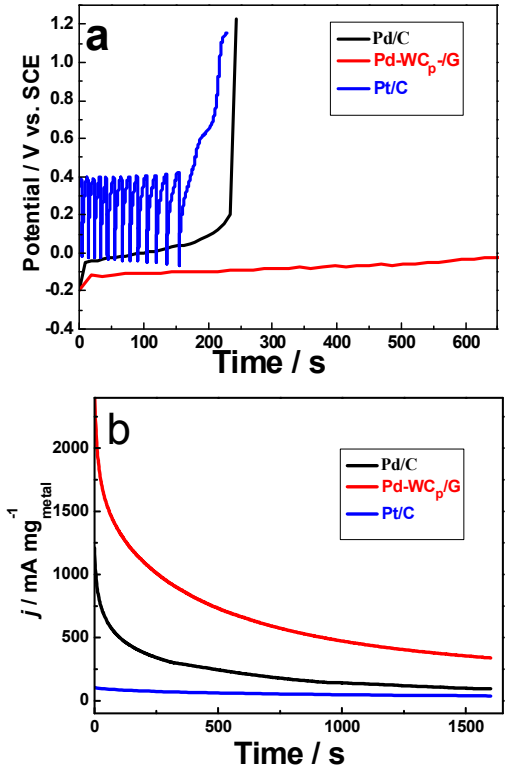

Fig. 8 (a) The chronopotential curves of of Pd/C, Pd-WC_P/G and Pt/C catalysts with anodic current density of 5 mA cm^{-2}, (b) chronoamperometric curves for the oxidation of formic acid catalyzed by Pd/C, Pd-WC_P/G and Pt/C at 0.3 V (*vs.* SCE) in N_2-saturated in 0.5 mol L^{-1} H_2SO_4 + 1.0 mol L^{-1} HCOOH solution.

The harsh operating environment in direct formic acid fuel cells (DFAFCs) call for extremely durable catalysts, and it is a great and open challenge to prepare catalysts to meet the required high durability criterion. With that in mind, The accelerated durability tests (ADT) of the Pd-WC_P/G and Pd/C catalysts were further carried out by continuous potentiodynamic sweep between -0.20 and 0.96 V (*vs.* SCE) in 0.5 mol L^{-1} H_2SO_4 + 1.0 mol L^{-1} HCOOH solution. Fig. 9a and 9b show the polarization curves for the formic acid oxidation on Pd-WC_P/G and Pd/C electrodes before and after the ADT. The peak current density of the Pd-WC_P/G after 2,000 cycles is 2700 mA mg^{-1}_{metal}, only a 12.2% loss. On the Pd/C electrode however, a current density of 198 mA mg^{-1}_{metal} was left with a loss of 55.5% in the formic acid oxidation activity. The ECSA analysis was done to understand the degraded performance. Fig. 9c and 9d compares the CVs of Pd-WC_P/G and Pd/C electrodes before and after ADT in N_2-saturated 0.5 mol L^{-1} H_2SO_4 solution, respectively. The Pd/C ECSA decreases to 57.2% after ADT (Fig. 9d) whereas the

Journal Name

Dynamic Article Links ►

Cite this: DOI: 10.1039/c0xx00000x

www.rsc.org/xxxxxx

ARTICLE TYPE

Pd-WC_P/G catalyst maintains 86.2% of the ECSA after 2,000 cycles ADT (Fig. 9c), consistent with the observed decrease of formic acid oxidation activity for respective catalysts. The ECSA loss of the catalysts is mainly due to agglomeration of Pd nanoparticles and passivized surface, which reduce the number of exposed Pd atoms and lower formic acid oxidation activities.

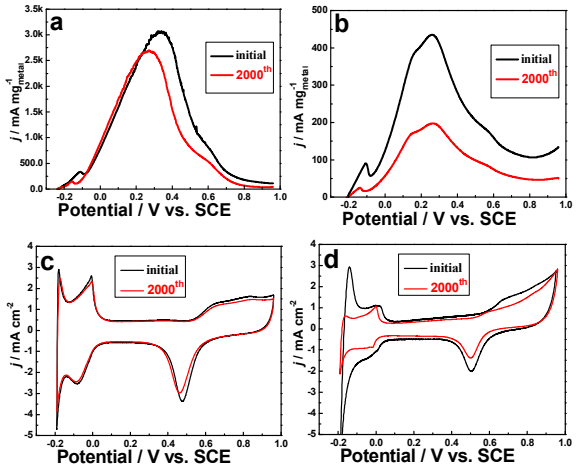

Fig. 9 Polarization curves for the formic acid oxidation on (a) Pd-WC_P/G and (b) Pd/C electrodes before and after the continuous CVs cycling test in N_2-saturated in 0.5 mol L^{-1} H_2SO_4 + 1.0 mol L^{-1} HCOOH solution, the corresponding CVs of (c) Pd-WC_P/G and (d) Pd/C electrodes before and after ADT in N_2-saturated 0.5 mol L^{-1} H_2SO_4 solution.

Electron transfer from the W to C atoms accompanies formation of the WC. This change of electron density states should downshift the tungsten d-band center and increase the degree of the d-band filling, thereby increase the d-band density near the Fermi level and make it similar to the electronic structures of noble metals, i.e., Pt and Pd. The strain introduced by WC nanocrystal and electronic interaction between the WC and noble meal nanoparticles will change the surface *d*-band center of the noble metal, which is likely the physical origin of the enhanced formic acid oxidation performance of Pd-WC_P/G.[50] In order to determine the origin of this promotional effect of Pd-WC_P/G, XPS was applied to probe the electronic structure of Pd in Pd/C and Pd-WC_P/G. As shown in Fig. 10, the fitting of the of X-ray photo-electron spectroscopy (XPS) curves of Pd elements show two series of peaks: the lower binding energies corresponding to the $3d_{5/2}$ and $3d_{3/2}$ levels of metallic Pd metal (blue lines), and the higher binding energies correspond to the $3d_{5/2}$ and $3d_{3/2}$ state of Pd oxide in the Pd–O coordination bonds (green lines). The Pd 3d peaks of Pd-WC_P/G are shifted significantly compared to those of Pd/C by about 0.5 eV to a lower binding energy. This weakened 3d electron binding energy of Pd in Pd-WC_P/G is attributed to a partial electron transfer from WC_P to Pd, which increases the electron density of Pd and enhances penetration of outer-layer electrons to inner layer.[51] The charge transfer to the Pd surface from the surface WC_P substantially reduces the surface binding strength of specific intermediates, lowering the activation energy of adsorbed HCOOH ($HCOOH_{abs}$) oxidation and leading to the enhanced activity toward formic acid oxidation. In addition to the electronic effect, WC_P may also directly participate in formic acid oxidation as WC has been reported as an effective hydrogen evolution catalyst.[52, 53] The hydrogen adsorption on the WC surface is facile, which may accelerate formic acid oxidation in a fashion similar to the hydrogen spill-over effect.[52, 54] Furthermore, WC supports could provide stronger electronegativity to the noble metals through an electron donating effect, which is beneficial to lowering CO adsorption on the noble metal surface, greatly improving the resistant to CO.[55]

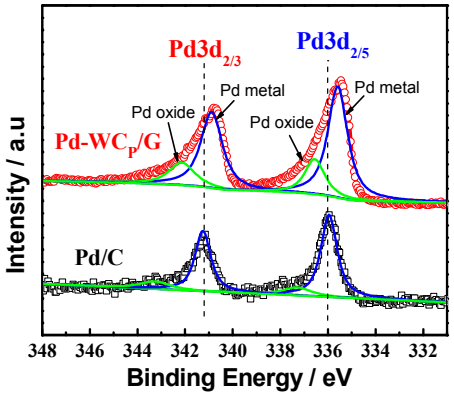

Fig. 10 XPS spectra of the Pd 3d region for Pd/C and Pd-WC_P/G.

X-Ray absorption measurement was carried out to elucidate the electronic structure and chemical environment of the Pd-WC_P/G. Both a reference Pd foil and the Pd/C were also measured for comparison. Fig. 11a shows the normalized X-ray absorption near-edge structure (XANES) spectra at the Pd *K*-edge for the Pd/C, Pd-WC_P/G and the Pd foil standard. The XANES spectrum of the Pd foil shows two distinct peaks at around 24365 and 24390 eV, corresponding to the allowed 1s → 5p transition.[56] The shapes of the XANES spectra and the edge position of Pd/C and Pd-WC_P/G resembled those of Pd foil, suggesting that the oxidation state of Pd in these two samples was almost Pd^0. More detailed inspection revealed that the two characteristic peaks of 1s → 5p transition in the Pd/C and Pd-WC_P/G seem a little weaker than those of Pd foil. This suggests that the Pd metal fcc structure in the Pd/C and Pd-WC_P/G is slightly disordered, likely due to their exposure to the surface. In the Fourier transforms (FT) of k^3-weighted Pd *K*-edge extended X-ray absorption fine structure (EXAFS) spectra of Pd/C and Pd-WC_P/G (Fig. 11b), both the Pd/C and the Pd-WC_P/G exhibit a single peak at

Journal Name

Dynamic Article Links ►

Cite this: DOI: 10.1039/c0xx00000x

www.rsc.org/xxxxxx

ARTICLE TYPE

approximately 2.5 Å, which is assigned to the closest neighbor Pd–Pd metallic bond. We fitted the Fourier transformation of the k^3-weighted EXAFS oscillations by a Pd–Pd model using the Artemis program in the IFEFFIT software package over the range of 3.0–14.3 $Å^{-1}$ to obtain a radial distribution function (RDF) and estimate the Pd coordination number. The obtained values of 6.9 and 6.4 for the Pd/C and the Pd-WC_P/G are smaller than that of the standard Pd foil (N =12), consistent with formation of small metal particles dispersed on the support. Of particular interest is using the EXAFS data to derive the Pd–Pd bond length of the catalyst. We note that the lengths of the Pd-Pd bond obtained for Pd-WC_P/G ($R_{Pd–Pd}$ =2.73 Å) is shorter than that of Pd/C ($R_{Pd–Pd}$ =2.75Å). This indicates the formation of non-covalent binding between Pd and WC_P/G providing unique coupling effects on electrochemical properties. The fitted parameters of the Pd/C, Pd-WC_P/G and Pd foil are summarized in Table 1.

Based on the above experimental results and analyses, the enhanced formic acid oxidation activity and superior stability of Pd-WC_P/G are attributed to the following factors: 1) electronic effect, the strong electronic interaction between Pd and WC_P promoting the oxidation of adsorbed HCOOH;[50] 2) bifunctional mechanism, the presence of residual oxygen functional groups on graphene sheets facilitating the oxidation of poisonous species CO_{abs} on active Pt sites;[44, 45] 3) the facile hydrogen adsorption on the surface of WC likely accelerating formic acid oxidation in a fashion similar to the hydrogen spill-over effect;[52, 54] 4) the presence of the WC reducing CO adsorption on the noble metals surface through an electron donating effect;[55] 5) graphene possessing high conductivity and making available one of the fastest electron transfer capabilities,[57, 58] providing fast electron transport during the reaction process; 6) large surface area of the graphene boosting the mass transfer and diffusion of the reactants and products.

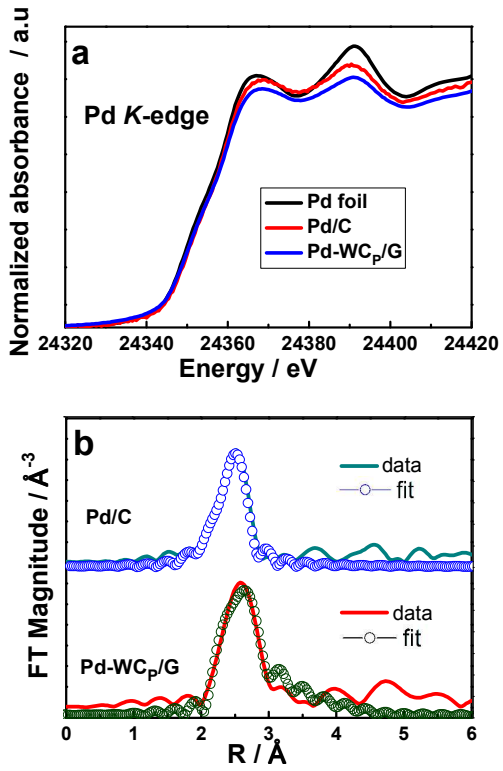

Fig. 11 (a) Pd *K*-edge XANES spectra for for Pd foil, Pd/C and Pd-WC_P/G, (b) k^3-weighted Pd *K*-edge EXAFS Fourier transform magnitudes and first-shell fit of the Pd *K*-edge obtained from the Pd/C and Pd-WC_P/G.

Table 1 Structural parameters determined by the curve-fitting analysis of Pd *K*-Edge EXAFS for the Pd/C, Pd-WC_P/G and Pd foil.

catalyst	*Pd edge energy (eV)*	R_{Pd-Pd}	N_{Pd-Pd}	*R factor*	σ^2
Pd/C	24350	2.75	6.9± 0.29	0.0012	0.0066± 0.0005
Pd-WC_P/G	24350	2.73	6.4± 0.55	0.0079	0.0091± 0.0008
Pd foil	24350	2.77	12.2 ± 1.2	0.00017	0.0058± 0.0004

Conclusions

In summary, hexagonal prism-shaped WC nanocrystals of 5 nm in size were successfully synthesized *via* a microwave assisting route. The WC_P nanocrystals were found dominated by $(01\bar{1}0)$, $(10\bar{1}0)$ and $(1\bar{1}00)$ facets with a preferred orientation of [0001]. Pd NPs were further loaded onto the WC_P/G to produce the Pd-WC_P/G catalyst, its electrochemical catalytic activity studied *via* formic acid oxidation. Compared to Pd/C, the Pd-WC_P/G display a remarkable promotion as catalyst for formic acid oxidation with an observed 7-fold increase in peak current density on Pd-WC_P/G electrode and significant enhancement in durability as well, making it a possible candidate for the next generation electrocatalyst in DFAFCs.

Journal Name

Dynamic Article Links ►

Cite this: DOI: 10.1039/c0xx00000x

www.rsc.org/xxxxxx

ARTICLE TYPE

Acknowledgements

This work was supported by the 100 Talents Project of Chinese Academy of Sciences, China (H9291440S3). Y. Qiu thanks the National Natural Science Foundation of China (No. 51206029). The authors thank beamline BL14W1 of Shanghai Synchrotron Radiation Facility (SSRF) for providing the beam time.

Notes and references

[a]*Dongguan Institute of Neutron Science (DINS), Dongguan Branch, Institute of High Energy Physics, Chinese Academy of Sciences,Dongguan 523808, China*
[b]*College of Chemistry and Environmental Engineering, Dongguan University of Technology, Guangdong 523808, P. R. China*
** e-mail: taoj@ihep.ac.cn (J. Tao); hechunyong@ihep.ac.cn (C. He).*

Corresponding Author

** e-mail: taoj@ihep.ac.cn (J. Tao); hechunyong@ihep.ac.cn (C. He).*

1. X. Yu and P. G. Pickup, *J. Power Sources*, 2008, **182**, 124-132.
2. Y. Wang, H. Liu, L. Wang, H. Wang, X. Du, F. Wang, T. Qi, J.-M. Lee and X. Wang, *J. Mater. Chem. A*, 2013, **1**, 6839-6848.
3. N. M. Marković and P. N. Ross Jr, *Surf. Sci. Rep.*, 2002, **45**, 117-229.
4. F. J. Vidal-Iglesias, A. López-Cudero, J. Solla-Gullón and J. M. Feliu, *Angew. Chem. Int. Ed.*, 2013, **52**, 964-967.
5. W.-Y. Yu, G. M. Mullen, D. W. Flaherty and C. B. Mullins, *J. Am. Chem. Soc.*, 2014, **136**, 11070-11078.
6. V. Mazumder, Y. Lee and S. Sun, *Adv. Funct. Mater.*, 2010, **20**, 1224-1231.
7. K. Jiang and W.-B. Cai, *Appl. Catal., B : Environ.*, 2014, **147**, 185-192.
8. W. Yuan, Y. Cheng, P. K. Shen, C. M. Li and S. P. Jiang, *J. Mater. Chem. A*, 2015, **3**, 1961-1971.
9. G. Samjeské and M. Osawa, *Angew. Chem. Int. Ed.*, 2005, **117**, 5840-5844.
10. H. Okamoto, W. Kon and Y. Mukouyama, *J. Phys. Chem. B*, 2005, **109**, 15659-15666.
11. J. Kim, C. Jung, C. K. Rhee and T.-h. Lim, *Langmuir*, 2007, **23**, 10831-10836.
12. C. Xu, Q. Hao and H. Duan, *J. Mater. Chem. A*, 2014, **2**, 8875--8880.
13. M. Liao, Y. Wang, G. Chen, H. Zhou, Y. Li, C.-J. Zhong and B. H. Chen, *J. Power Sources*, 2014, **257**, 45-51.
14. S.-Y. Lee, N. Jung, J. Cho, H.-Y. Park, J. Ryu, I. Jang, H.-J. Kim, E. Cho, Y.-H. Park, H. C. Ham, J. H. Jang and S. J. Yoo, *ACS Catal.*, 2014, **4**, 2402-2408.
15. D. Xu, S. Bliznakov, Z. Liu, J. Fang and N. Dimitrov, *Angew. Chem. Int. Ed.*, 2010, **49**, 1282-1285.
16. L. Zhang, S.-I. Choi, J. Tao, H.-C. Peng, S. Xie, Y. Zhu, Z. Xie and Y. Xia, *Adv. Funct. Mater.*, 2014, **24**, 7520-7529.
17. Y. She, Z. Lu, W. Fan, S. Jewell and M. K. H. Leung, *J. Mater. Chem. A*, 2014, **2**, 3894-3898.
18. B. T. Sneed, A. P. Young, D. Jalalpoor, M. C. Golden, S. Mao, Y. Jiang, Y. Wang and C.-K. Tsung, *ACS Nano*, 2014, **8**, 7239-7250.
19. F. Lan, D. Wang, S. Lu, J. Zhang, D. Liang, S. Peng, Y. Liu and Y. Xiang, *J. Mater. Chem. A*, 2013, **1**, 1548-1552.
20. B. Zhang, H. Peng, L. Yang, H. Li, H. Nan, Z. Liang, H. Song, H. Su, C. Li and S. Liao, *J. Mater. Chem. A*, 2015, **3**, 973-977.
21. Y. Tang, R. E. Edelmann and S. Zou, *Nanoscale*, 2014, **6**, 5630-5633.
22. S. Yang, C. Shen, Y. Tian, X. Zhang and H.-J. Gao, *Nanoscale*, 2014, **6**, 13154-13162.
23. J. Matos, A. Borodzinski, A. M. Zychora, P. Kedzierzawski, B. Mierzwa, K. Juchniewicz, M. Mazurkiewicz and J. C. Hernández-Garrido, *Appl. Catal., B : Environ.*, 2015, **163**, 167-178.
24. J. Chang, L. Feng, C. Liu, W. Xing and X. Hu, *Angew. Chem. Int. Ed.*, 2014, **53**, 122-126.
25. H. Meng and P. K. Shen, *Chem. Commun.*, 2005, 4408-4410.
26. C. He and P. K. Shen, *Nano Energy*, 2014, **8**, 52-61.
27. C. He, H. Meng, X. Yao and P. K. Shen, *Int. J. Hydrogen Energy*, 2012, **37**, 8154-8160.
28. M. Shi, W. Liu, D. Zhao, Y. Chu and C. a. Ma, *J. Solid State Electrochem.*, 2014, **18**, 1923-1932.
29. D. V. Esposito, S. T. Hunt, A. L. Stottlemyer, K. D. Dobson, B. E. McCandless, R. W. Birkmire and J. G. Chen, *Angew. Chem. Int. Ed.*, 2010, **49**, 9859-9862.

Journal Name

Dynamic Article Links ►

Cite this: DOI: 10.1039/c0xx00000x

www.rsc.org/xxxxxx

ARTICLE TYPE

30. Y. Yan, L. Zhang, X. Qi, H. Song, J.-Y. Wang, H. Zhang and X. Wang, *Small*, 2012, **8**, 3350-3356.

31. J. B. d'Arbigny, G. Taillades, M. Marrony, D. J. Jones and J. Rozière, *Chem. Commun.*, 2011, **47**, 7950-7952.

32. Y. Sun, H. Cui, S. X. Jin and C. X. Wang, *J. Mater. Chem.*, 2012, **22**, 16566-16571.

33. Z. Yan, M. Cai and P. K. Shen, *Sci. Rep.*, 2013, **3**, 1646.

34. L. Bischoff, S. Hausmann, M. Voelskow and J. Teichert, *Nucl. Instr. and Meth. in Phys. Res. B*, 1999, **147**, 327-331.

35. K. M. Ø. Jensen, M. Christensen, H. P. Gunnlaugsson, N. Lock, E. D. Bøjesen, T. Proffen and B. B. Iversen, *Chem. Mater.*, 2013, **25**, 2282-2290.

36. O. L. Krivanek, M. F. Chisholm, V. Nicolosi, T. J. Pennycook, G. J. Corbin, N. Dellby, M. F. Murfitt, C. S. Own, Z. S. Szilagyi, M. P. Oxley, S. T. Pantelides and S. J. Pennycook, *Nature*, 2010, **464**, 571-574.

37. B. Goris, S. Bals, W. Van den Broek, E. Carbó-Argibay, S. Gómez-Graña, L. M. Liz-Marzán and G. Van Tendeloo, *Nat. Mater.*, 2012, **11**, 930-935.

38. F. Banhart, J. Kotakoski and A. V. Krasheninnikov, *ACS Nano*, 2010, **5**, 26-41.

39. L. Cançado, A. Reina, J. Kong and M. Dresselhaus, *Phys. Rev. B*, 2008, **77**, 245408.

40. A. N. Obraztsov, A. V. Tyurnina, E. A. Obraztsova, A. A. Zolotukhin, B. Liu, K.-C. Chin and A. T. S. Wee, *Carbon*, 2008, **46**, 963-968.

41. Y. Xing, *J. Phys. Chem. B*, 2004, **108**, 19255-19259.

42. W. Pan, X. Zhang, H. Ma and J. Zhang, *J. Phys. Chem. C*, 2008, **112**, 2456-2461.

43. R. Li, Z. Wei, T. Huang and A. Yu, *Electrochim. Acta*, 2011, **56**, 6860-6865.

44. M. S. El-Deab, A. M. Mohammad, G. A. El-Nagar and B. E. El-Anadouli, *J. Phys. Chem. C*, 2014, **118**, 22457-22464.

45. M. Krausa and W. Vielstich, *J. Electroanal. Chem.*, 1995, **399**, 7-12.

46. P. Justin and G. Ranga Rao, *Int. J. Hydrogen Energy*, 2011, **36**, 5875-5884.

47. X. Yu and P. G. Pickup, *Electrochem. Commun.*, 2009, **11**, 2012-2014.

48. J. Kua and W. A. Goddard, *J. Am. Chem. Soc.*, 1999, **121**, 10928-10941.

49. S. Sharma, A. Ganguly, P. Papakonstantinou, X. Miao, M. Li, J. L. Hutchison, M. Delichatsios and S. Ukleja, *J. Phys. Chem. C*, 2010, **114**, 19459-19466.

50. Y. Liu, T. G. Kelly, J. G. Chen and W. E. Mustain, *ACS Catal.*, 2013, **3**, 1184-1194.

51. D. J. Ham, C. Pak, G. H. Bae, S. Han, K. Kwon, S.-A. Jin, H. Chang, S. H. Choi and J. S. Lee, *Chem. Commun.*, 2011, **47**, 5792-5794.

52. M. C. Weidman, D. V. Esposito, I. J. Hsu and J. G. Chen, *J. Electrochem. Soc.*, 2010, **157**, 179-188.

53. W.-F. Chen, J. T. Muckerman and E. Fujita, *Chem. Commun.*, 2013, **49**, 8896-8898.

54. K.-W. Park, K.-S. Ahn, Y.-C. Nah, J.-H. Choi and Y.-E. Sung, *J. Phys. Chem. B*, 2003, **107**, 4352-4355.

55. G. Cui, P. K. Shen, H. Meng, J. Zhao and G. Wu, *J. Power Sources*, 2011, **196**, 6125-6130.

56. T. Hara, J. Sawada, Y. Nakamura, N. Ichikuni and S. Shimazu, *Catal. Sci. Technol.*, 2011, **1**, 1376-1382.

57. E. McCann and V. I. Fal'ko, *Phys.Rev. Lett.*, 2006, **96**, 086805.

58. C. Berger, Z. Song, X. Li, X. Wu, N. Brown, C. Naud, D. Mayou, T. Li, J. Hass, A. N. Marchenkov, E. H. Conrad, P. N. First and W. A. de Heer, *Science*, 2006, **312**, 1191-1196